




# Computationally optimize microstructural investigation of austenitic steels for high strength–toughness properties

Muhammad Raies Abdullah<sup>1</sup>, Fang Liang<sup>1,2,\*</sup> , Cai Hongneng<sup>1</sup>, and Wie Ren<sup>1</sup>

<sup>1</sup>State Key Laboratory for Mechanical Behavior of Materials, Xi'an Jiaotong University, Xi'an 710049, China

<sup>2</sup>School of Mechanical and Electrical Engineering, Xiamen University Tan Kah Kee College, Zhangzhou 363105, China

**Received:** 31 May 2022

**Accepted:** 5 November 2022

**Published online:**  
1 January 2023

© The Author(s), under exclusive licence to Springer Science+Business Media, LLC, part of Springer Nature 2022

## ABSTRACT

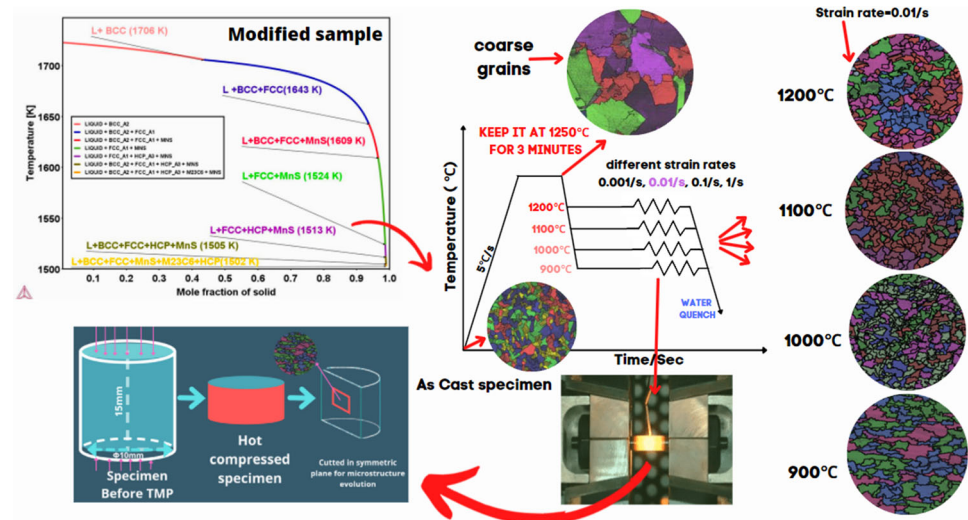
Austenitic steel has been the backbone of the nuclear reactor industry for power generations for many decades. 304 Steel alloy with the minimal amount of nitrogen and carbon was designed based on the different alloying composition systems for traditional high strength–toughness combinations and longevity for high-temperature applications. At elevated temperatures, the combination of strength–toughness deteriorated by metallic phases and coarsening of carbides. Chromium increases oxidation and corrosion resistance; however, brittle intermetallic compounds can develop in the resultant alloys when the Cr level rises, resulting in low ductility. First, Calphad strategical optimization was used for alloying composition and processing parameters for high temperature and pressure applications using Thermocalc and Jmat-Pro software packages. Second, to increase strength–toughness combination, isothermal deformation for different strain rates ( $0.001\text{--}1\text{ s}^{-1}$ ) with different deformation temperatures ( $900\text{--}1200\text{ °C}$ ) was applied. It was also proven that different dynamic recrystallization (DRX) mechanisms caused different grain size evolutions, and the dividing point was estimated to be  $0.1\text{ s}^{-1}$  strain rate at high deformation temperatures.

Handling Editor: Ghanshyam Pilania.

Address correspondence to E-mail: fangl@xjtu.edu.cn

<https://doi.org/10.1007/s10853-022-07933-y>

## GRAPHICAL ABSTRACT



## Introduction

Austenitic stainless steel offers a wide range of commercial uses and is commonly utilized in basic structural-property combinations because it is stable even at room temperature. In this era of advanced power generation like nuclear power industries, hot forging is an essential method for producing critical structural elements of austenitic stainless steel [1–4]. 304 austenitic stainless steel is a widely used corrosion-resistant steel. However, it is easy to precipitate carbides along the grain boundary during processing and service, which increases intergranular stress corrosion cracking (IGSCC) in boiling water reactors (BWRs) [5]. Nitrogen and nickel stabilized the austenitic phase zone. The strength–toughness combination of steel and intergranular corrosion resistance can be improved by reducing the C content and adding an appropriate amount of N. This kind of steel is called nitrogen-controlled (304NG) stainless steel [6]. Because of its comprehensive mechanical properties, resistance to neutron radiation embrittlement and corrosion resistance are widely used in pressure water reactor (PWR) internal components. These internal

components mainly include various forgings, thermomechanical processing (TMP), and processed forming parts of plates, bars, and pipes [1, 3]. DRX is essential in the thermoplastic forming process, causing various changes in the structure of the deformed metal, thereby affecting the mechanical, physical, and chemical properties of the material. Discontinuous and continuous DRX processes are the most common DRX mechanisms (DDRX and CDRX, respectively) [7]. DDRX is caused by local grain boundary bulging, resulting in DRX grains producing, which utilize work-hardened surrounds during deformation. The increment in sub-boundary misorientation is generated by the continual accumulation of dislocations triggered by the deformation in the CDRX mechanism results in the formation of new grains. In alloys with low stacking fault energy (SFE), such as austenitic stainless steel and Cu and Ni alloys, DDRX is considered to be the most predominant softening method [8]. Since austenitic stainless steel hardly undergoes phase transformation during hot working, recrystallization becomes a decisive factor affecting its final structure [7]. Therefore, studying its DRX behavior during hot deformation is essential for controlling the forming process and obtaining fine and uniform grain structures with great significance.

Its common knowledge that enhancing the strength of material reduces toughness and ductility; grain size reduction or refinement is the only approach to boost both characteristics with an identical pattern. It is self-evident that if you make the grain structure smaller, you put more impediments in the grain and thus in the dislocation, and hence the strength should increase, as the Hall–Petch equation implies [9]. In this work, two ways were discussed to improve toughness, i.e., thermodynamically (Calculation of phase diagrams) and mechanically (Thermomechanical processing). In the first part, CALPHAD strategies were used for optimizing alloying elements to minimize the detrimental phases like carbides and brittle metallic phases and predict the optimum concentrations of 304NG steel. The second part of refined grain distributions using thermomechanical processing (TMP) can be improved by refining the microstructure scale, eliminating hard particles that fracture easily, introducing ductile barriers to the propagation of cracks, and by mechanisms that damp the motion of cracks. The important role of precipitation or phase fractions in the success of excellent creep properties has been understood as well as comprehensively studied for a long time [10]. High- or low-temperature toughness applications of stainless steel decreased significantly when some intermetallic brittle phase ( $\sigma$ ) and  $M_{23}C_6$  carbides form at the boundaries of ferrite or inside the ferrite and austenite phase [11, 12].

Recently, several models have been proposed to elucidate the modification mechanisms of the alloying components of the 304 series to enhance its toughness, strength, and hardness. J. L. Marulanda et al. [13] deposit aluminide coating on AISI 304, having 18% Cr for higher steam generation plants to increase thermal efficiency, including reductions in carbon dioxide emissions and fuel consumption. Mn and Ni are added to improve the strength and fracture toughness of steels, while Ni has more significant influence than Mn on the properties of steel alloys [14]. Some researchers also worked on dynamic recrystallization of 304 steel, i.e., Wang studied the twinning evolution of austenitic stainless steel at different strain rates and its effect on dynamic recrystallization [7]. Wahabi et al. [15] studied the effect of initial grain size on dynamic recrystallization and predicted the nucleation sites for DDRX grains; meanwhile, Marchattiwat studied the progress of DRX on Avrami relation and work hardening data. Kim et al. conducted thermal torsion experiments on

304 stainless steel, determined peak and steady-state stress under different conditions, and analyzed the DRX using the Avrami equation Kinetics [16]. Many studies have used kinetic and microstructural exams to study toughness in high-temperature applications and creep rupture life in 304-grade steel. However, very few fundamental investigations have been carried out on secondary phases through thermodynamical optimization. The minimal amount of alloying elements (Si, Cr, Mn, and Ni) and thermomechanical heating parameters that retain the largest percentage of austenite and have the ideal balance of hardness, strength, and toughness for high-temperature applications are the objectives of this study. Hot compression experiments at strain rates ranging from 0.001 to  $1\text{ s}^{-1}$  were used to evaluate the flow behavior and DRX processes for 304NG austenitic stainless steel. The findings should help researchers better understand the impact of strain rates on DRX developments and give useful recommendations for processing design.

### Computational design for alloying elements

The alloy chemistry design pattern emphasized phase fraction behavioral studies and their implications on structural and mechanical qualities. The CALPHAD technique was used to properly characterize the influence of phases throughout 304NG steel related to different concentrations of Cr, Ni, Mn, and Si. Two well-known CALPHAD-based software packages were used to optimize alloying compositions for numerous 304NG steel specimens. In combination with Thermo-Calc® using the TCFE9 database, calculations have been carried out to the individual phases ( $\gamma$ -FCC,  $\alpha$ -BCC,  $M_{23}C_6$ , Sigma, and G-Phase). Many mechanical properties like hardness, strength, and Young's modulus of alloy w.r.t different compositions of Mn, Si, Ni, and Cr by comparing their yield, tensile strengths were predicted by Jmatpro software. This tool has been proven helpful in understanding the basic trend of mechanical characteristics [17–20]. For mechanical calculations related to 304NG analysis, it was assumed that the  $\gamma$ -FCC grain size is 10–15  $\mu\text{m}$ , and calculations were performed at room (300 K) temperature.

Austenite stabilizers such as Nb, Mn, and Ni are well known for increasing the quantity of retained austenite (RA), decreasing the martensite initiation

temperature, in addition to increasing the stacking fault energy (SFE). A greater concentration of C (> 0.2 wt%) reduces weldability and increases susceptibility to hydrogen cracking. Ni content should be kept to a minimum because of the high expense; furthermore, it inhibits carbide precipitation and enhance carbon partitioning into retained austenite (RA), hence increasing its stability. Nevertheless, the use of Si above 0.5 wt% produces complications in hot-dip galvanization and continuous casting and welding. When solid solution hardening is used in the presence of Nb, high-temperature strength can rise. When steel is utilized at high temperatures of about 900 °C for a long time, the solute Nb readily precipitates out as carbonitride. As a result of the Nb precipitation, the high-temperature strength may be altered. Thermocalc database is valid for simulating the solidification process, matrix phase stability ( $\gamma$ -Fcc and  $\alpha$ -Bcc), precipitation of secondary phases such as sulfides and carbides, and intermetallic phases such as Sigma and G-Phase [21]. Table S1 contains the standard composition of 304NG and different types of modified compositions of the same alloy with different compositions w.r.t Cr, Ni, Si, and Mn [22]. The alloying composition range is as follows; chromium is between 18 and 20 wt%, Ni is about 8–11 wt%, while S and P are in minimal concentration [23, 24]. The composition of Mn and Si is (0.81–1.5 wt%) and (0.47–1 wt%), respectively, as shown in.

## Result and discussion

### Thermodynamic simulations of 304NG steel

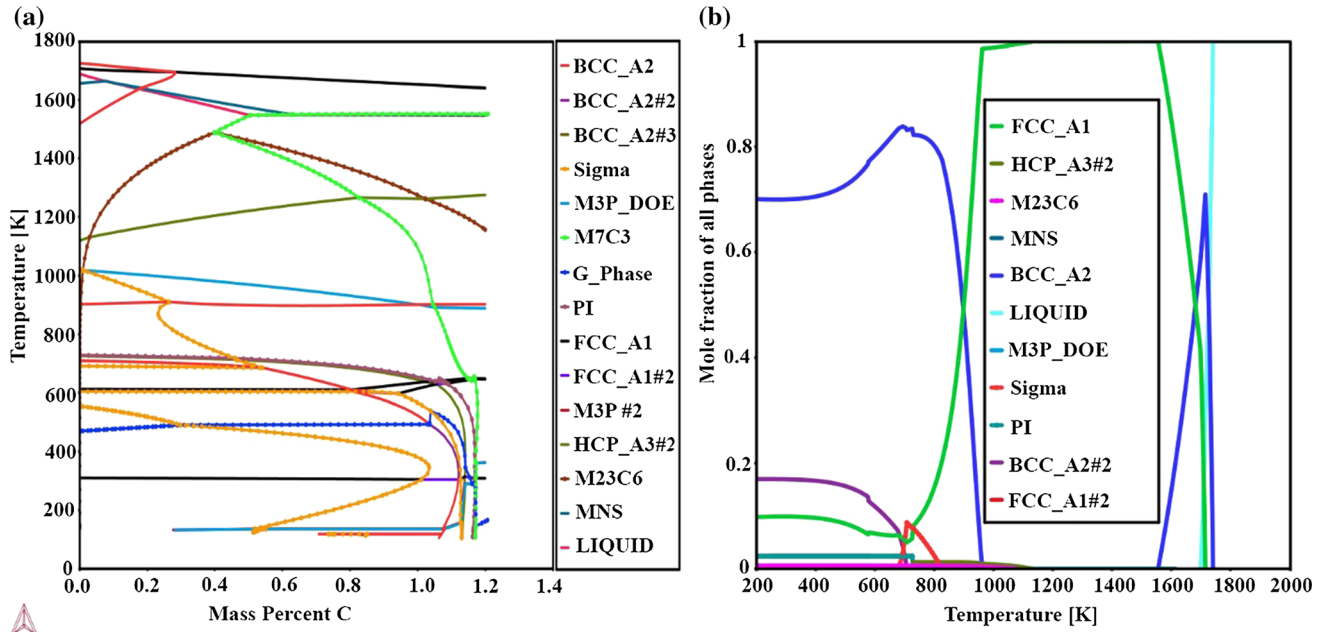
The phase fractions of 304NG steel specimens were calculated using Thermocalc, i.e., austenite (FCC\_A1), ferrite(BCC\_A2), carbides ( $M_{23}C_6$ ,  $M_7C_3$ ), and intermetallic phases like Sigma( $\sigma$ ) and G-phase by changing the composition of C wt% in 304NG steel as shown in Fig. 1a. Low amounts of C were examined according to ASTM standards, this computational part of the work mainly focused on  $\gamma$ , ferrite, carbides, and intermetallic phases as shown in Fig. 1b. In 304NG, some elements are  $\gamma$ -Fcc formers, e.g., C, Ni, Mn [30], and some  $\gamma$ -Fcc stabilizers are, for example, Ni and Mn [25]. Sigma( $\sigma$ ) phase occurs at 600–900 °C temperatures depending on elemental compositions of Cr, Ni, Si, and Mn, which enhance its stability [26] shown in Fig. 1b. The diffusion of

chromium in  $\alpha$ -BCC is an essential thermodynamic process in the formation of the Sigma( $\sigma$ ) phase. The  $\sigma$  phase composition in austenitic stainless steels can be written out as  $(Fe, Ni)_3(Cr, Mo)_2$  [27].

Sigma( $\sigma$ ) precipitate is an essential phase in several series of stainless steels, is one of the main factors for many mechanical properties, corrosion resistance, weldability, and hardness [28]. The  $Ac_3$  ( $\alpha \rightarrow \gamma$ ) and  $A_4$  ( $\gamma \rightarrow \delta$ ) are critical temperatures for phase transformations, as shown in Fig. 1b. At  $A_4$  temperature, higher solubility of phosphorus and sulfur is found in the  $\delta$ -phase than in the  $\gamma$  phase, resulting in an increase in ductility due to the suppression of grain boundary segregation. When the degree of  $\delta$ -ferrite is as high as 7–10%, however, ductility suffers dramatically due to the strain concentration at the interface caused by a difference in deformation resistance between  $\gamma$  and  $\delta$  phase. As a result, controlling the  $\delta$ -ferrite is critical for reducing defects associated with hot working [29]. Figure 1b shows that all phases for baseline samples for 304NG specimens, including secondary precipitates, have a detrimental effect on the toughness and ductility of the specimens in high-temperature applications.

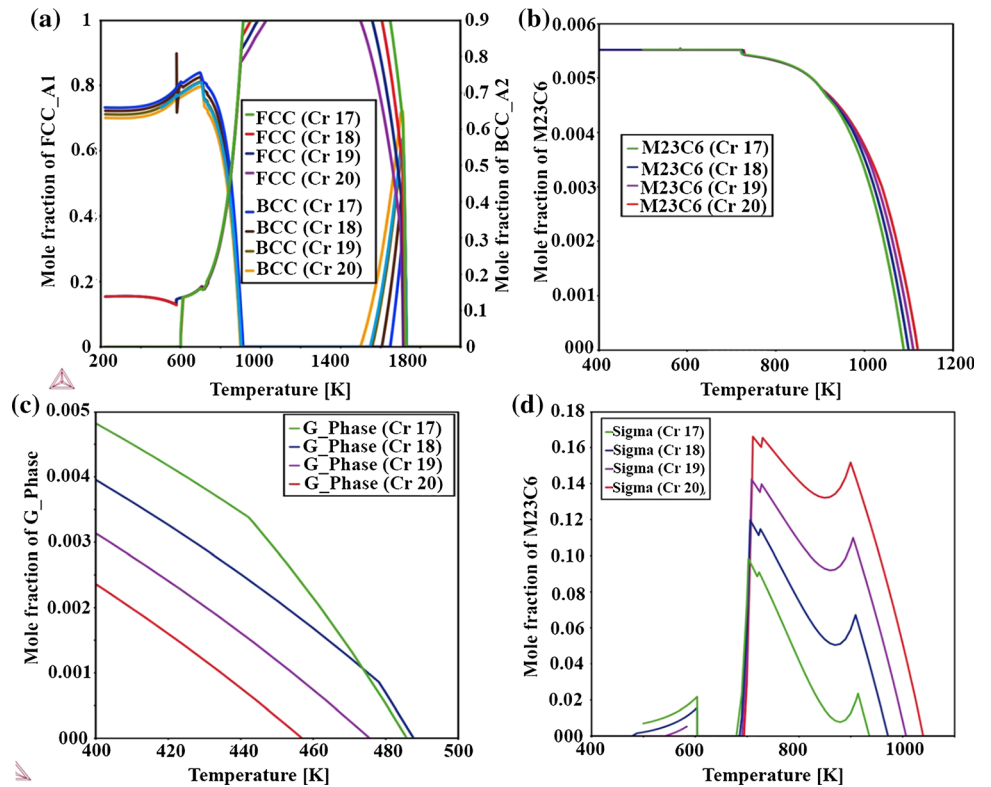
### The effects of different alloying elements (Cr, Mn, Si, Ni) on Phases

Figure 2 illustrates the phase transformations for different Cr concentrations of 17–20 wt%. As shown in Fig. 2, Cr has different effects on different phases. Significant phase stabilities are observed for  $\alpha$ ,  $\gamma$ ,  $\delta$ ,  $M_{23}C_6$ , *sigma*, and G-phase with changing Cr concentration. Chromium raises the eutectoid temperature, shrinking the  $\gamma$ -Fcc phase-field shown in Fig. 2a. At high temperatures, the reduction of Cr tends to shrink the  $\delta$  phase along with increasing  $A_4$  temperature. As shown in Fig. 2a, increasing the Cr concentration lowers the  $Ac_3$  temperature along with molar fraction of the ferrite phase. Cr increases the stability as well as molar fraction till 700 to 1050 K temperature for most deleterious hard and brittle *sigma* phase w.r.t toughness at high temperature and pressure applications [30]. Increasing Cr content increases the  $M_{23}C_6$  carbide stability at high temperatures (1080–1115 K), which matched the previous literature [31, 32]. Because  $M_{23}C_6$  has a higher coarsening rate at high temperatures, causing the Ostwald ripening effect, an increase in  $M_{23}C_6$  carbide has detrimental effects on ductility and toughness at



**Figure 1** a Phase calculations of 304NG specimen w.r.t to changing Carbon composition at 200 K to 2000 K b Property diagram for different phases in the baseline specimen..

**Figure 2** Effect of Cr concentration in 304NG  
a austenite and ferrite phases,  
b  $M_{23}C_6$ , c G-phase, and  
d Sigma phase..



higher temperatures [33]. The stability of G-phase reduces with increasing Cr content in 304NG alloys, as shown in Fig. 2c. Well, 304NG is a class of austenitic steel in which the parent phase is austenite, but

Cr tends to stabilize ferrite phase and increase both  $A_{c3}$  and  $A_{4}$  points to a higher temperature, so overall increasing Cr is not beneficial for high-temperature applications; therefore, minimizing the Cr content is

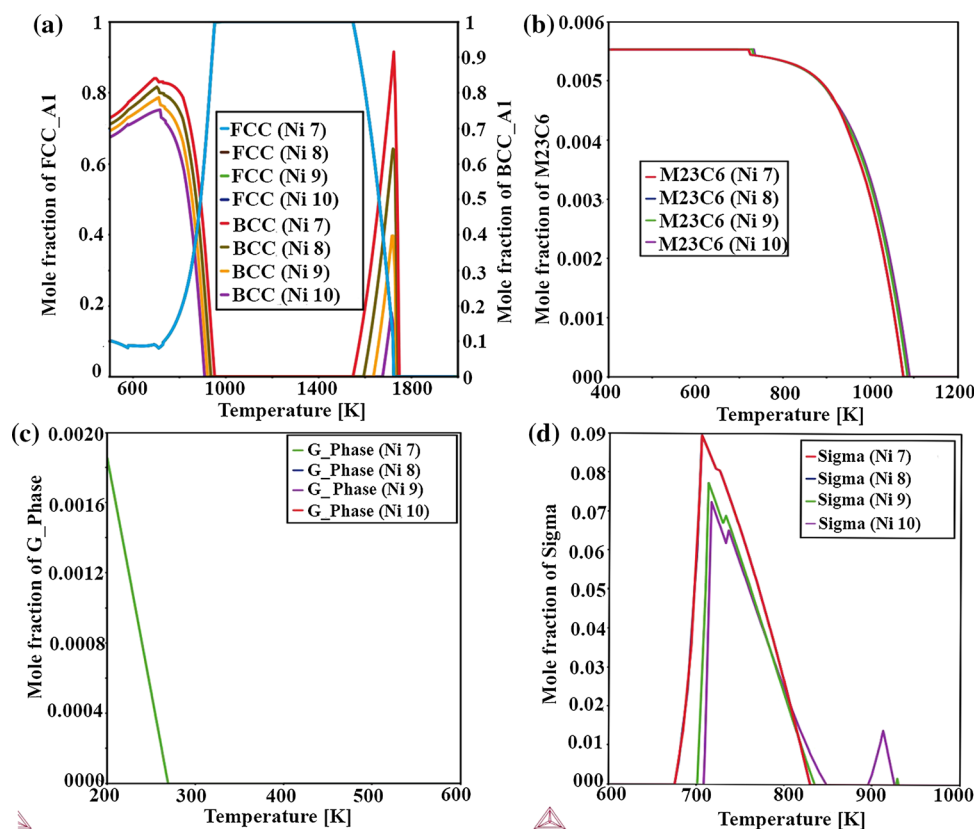
necessary. The accumulation of  $\sigma$  phase, on the other hand, has become a substantial issue; even a small proportion of this  $\sigma$  phase causes a severe loss of toughness and ductility, a phenomenon known as  $\sigma$  phase embrittlement. As for the problem of increasing critical temperatures ( $A_{c3}$  and  $A_4$ ) comes from the prospect of growing the stability of undesirable phase transformations during TMP, which could reduce its toughness at high and low-temperature applications. However, because Cr promotes high oxidation and corrosion resistance in 304NG, proper application-wise optimization of oxidation, corrosion resistance, and toughness is required for the material to function properly. Figure S2c, d (supplementary material) illustrates that increasing Cr concentrations increases the strength and hardness but decreases young's modulus of 304NG specimens.

Figure 3 shows the phase transformations of 304NG w.r.t Ni concentrations of 8–11wt%. As shown in Fig. 3, Ni has different effects on different phases. Ni stabilizes an austenitic structure because of increasing intrinsic matrix toughness and ductility and facilitating cross-slip at lower temperatures. It also decreases the corrosion rate and is thus beneficial

in acid environments, improves the oxide stability, has high capacity alloying for other materials, and is resistant to Carbon, nitrogen, and halogens [34, 35]. As shown in Fig. 3a, increasing Ni content tends to decrease the stability of the  $\alpha$  phase along with reducing the  $\delta$  phase. It lowers the  $A_{c3}$  temperature along with decreasing the molar fraction of the  $\alpha$ -ferrite phase, which is suitable for toughness and ductility. Ni concentration decreases the molar fraction of Sigma phase stability shown in Fig. 3d between 670 to 950 K temperature range. Ni increases the stability of  $M_{23}C_6$  phase at 1080–1090 K and reduces its molar fraction. Nickel is also utilized to make intermetallic compounds that boost the strength of hardening steels during precipitation [34]. G-phase has complex behavior for Ni dependent samples, i.e., shows stability at 7 wt only as shown in Fig. 3c. Nickel stabilizes  $\gamma$  by increasing the activity of carbon and promoting C partitioning responsible for the decomposition of retained  $\gamma$  is delayed to higher temperatures [28].

However, considering that an increase of Ni is good for toughness, but also has limitations like combining with sulfur to make sulfides have low melting eutectic; so proper optimization could be

**Figure 3** Effect of Ni concentration in 304NG  
a austenite and ferrite phases,  
b  $M_{23}C_6$ , c G-phase, d Sigma phase..



needed w.r.t more alloying elements like cobalt to reduce this issue in high-temperature applications. Figure S2c, d (supplementary material) illustrates that increasing Ni concentrations increases the strength, hardness, and Young’s modulus of 304NG specimens.

Figure 4 depicts phase transitions for Mn concentrations ranging from 0.8 to 1.4 wt%. Manganese is widely added to boost the hot ductility of steel alloys. Figure 4a illustrates that its impact on the  $\alpha/\gamma$  balance changes with temperature. At low temperatures up to 1000 K, Mn acts as an austenite stabilizer and lowers  $A_{c3}$  temperature of the alloy. Regarding  $M_{23}C_6$  carbide, changing Mn’s content does not change the stability. As shown in Fig. 4d, the higher molar fraction of  $\sigma$  phase is at 700–800 K temperature; increasing Mn concentration shrinks the stability temperature range of  $\sigma$  phase. Manganese sulfide inclusions improve machinability and retarding grain growth in steels and are not suitable for corrosion resistance [36]. G-phase still has complex behavior for Mn contents, although Mn increases the stability of G-phase at higher temperature range till 550 K as shown in Fig. 4d. MnS inclusions, as a stress raiser, have a soft nature, low shear strength, and high ductility, which reduces steel cutting resistance and tool wear [37]. Figure S1c, d (supplementary material) illustrates that increasing Mn concentrations

decreases the hardness and young’s modulus of 304NG specimens.

Figure 5 depicts the phase transitions of 304NG compared to Si concentrations of 0.45–1 wt%. At both high and low temperatures, Si is a robust oxidizer. At high temperatures, such as 1580–1760 K, it promotes a  $\delta$ -ferritic structure, as illustrated in Fig. 5a. Regarding  $A_{c3}$  and  $A_{c4}$  temperatures, changing silicon does not affect the  $A_{c3}$  and  $A_{c4}$  temperatures. As shown in Fig. 5b, Si reduces the molar fraction of  $M_{23}C_6$  and increases the molar fraction of the inter-metallic  $\sigma$  phase; the highest molar fraction is at around 700 K, as depicted in Fig. 5d. G-phase stability in 304NG steel reliant mainly on Si content; more Si content enhances G-phase stability at higher temperatures, such as 400–675 K, as illustrated in Fig. 5c. Si is also a useful alloying element in steel to lower density [40] and prevents cementite from  $\gamma$  becoming enriched with carbon, which is retained in the final precipitates [27].

Carbides are eliminated using Silicon in steel, instead of precipitating as cementite C is rejected into the residual austenite, stabilizing it down to an ambient temperature. The resulting microstructures are carbon-enriched regions of  $\gamma$  phase [38]. Figure S1a, b (supplementary material) illustrates that increasing silicon concentrations in 304NG specimens increases the hardness and decreases the specimens’

**Figure 4** Effect of Mn concentration in 304NG  
**a** austenite and ferrite phases,  
**b**  $M_{23}C_6$ , **c** G-phase, **d** Sigma phase..

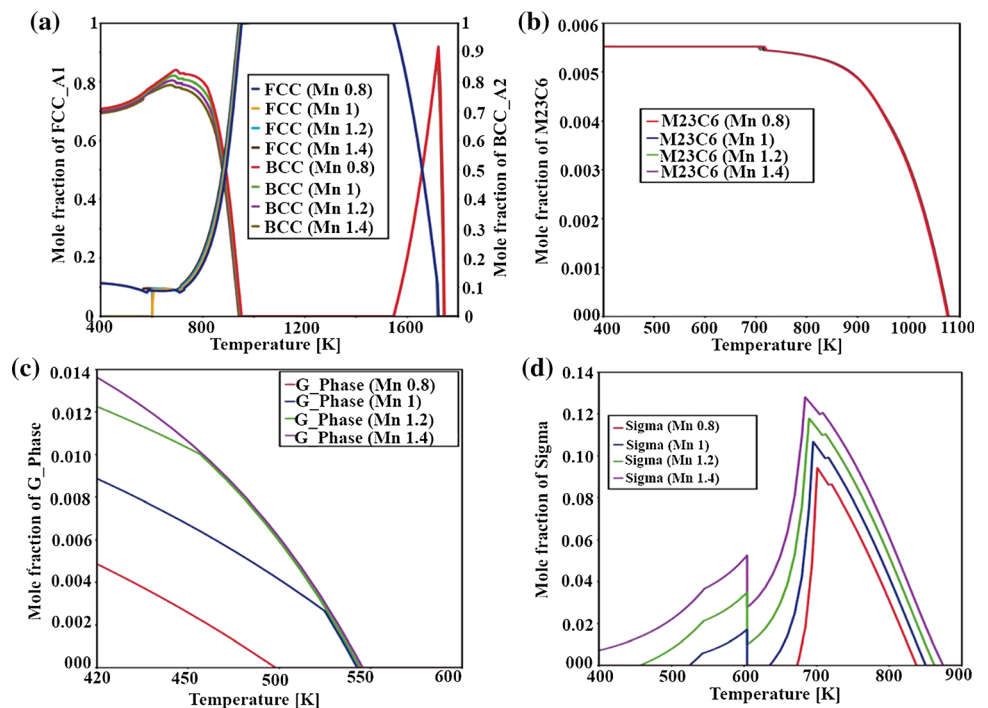
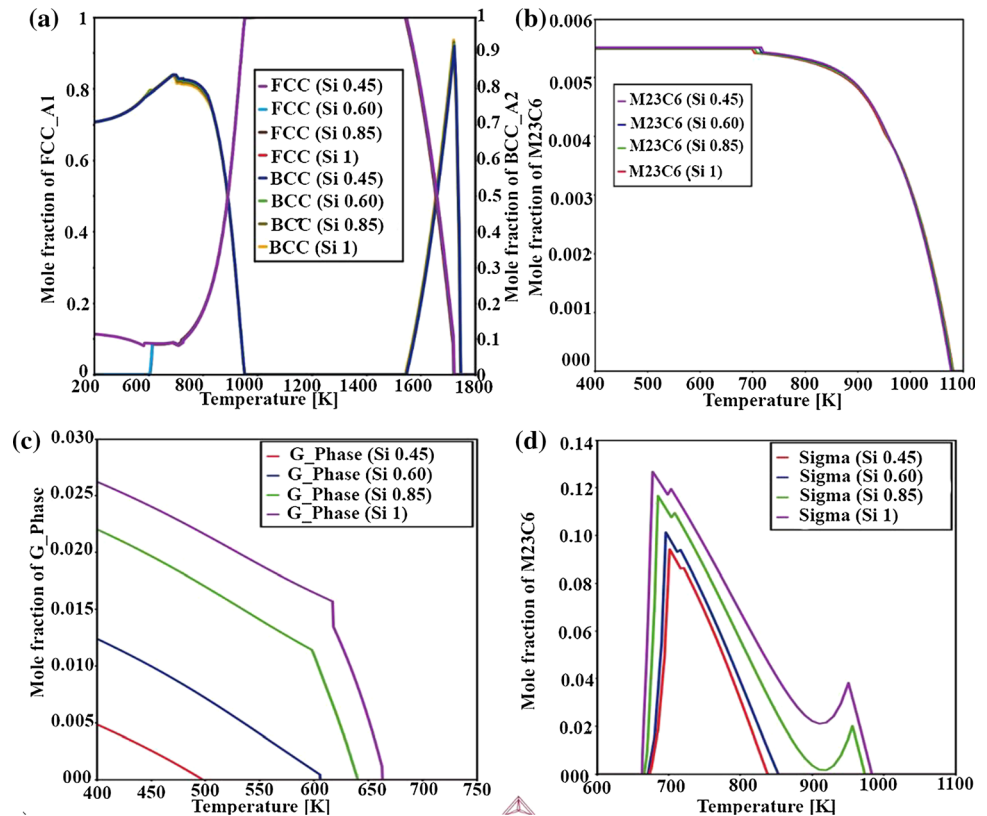


**Figure 5** Effect of Si concentration in 304NG  
 a austenite and ferrite phases,  
 b  $M_{23}C_6$ , c G-phase, d Sigma phase..



young's modulus. Si content also increases the strengths because of G-phase or fine growth of particles. G-phase is an essential part of hindering the growth of cementite particles or making it finer or less in size in 304NG steel grade, which is estimated to enhance the hardness and strength of the steel [39]. However, high hardness is achieved by hard and stiff precipitations and the blockage of dislocations by strong point defects interaction, which is also responsible for an increase in the modulus [30]. It is well known that finely distributed  $M_{23}C_6$  carbide particles in the matrix may strengthen the austenitic stainless steels but also  $M_{23}C_6$  carbide is undesirable since its intergranular corrosion and decrease in ductility and toughness [12]. Paradoxically, the existence of  $M_{23}C_6$  on grain boundaries could make slip more difficult, boosting creep ductility [40]. In steels, MnS inclusions help to improve machinability while also slowing grain growth. Meanwhile, the shape of these sulfide inclusions has a significant impact on a variety of steel characteristics. Manganese sulfide also had a negative impact on steel alloy mechanical characteristics and corrosion parameters [36]. G-phase enhances strength and brittleness by

interacting with movable dislocations while decreasing toughness and ductility [41, 42].

Figure 6 shows the results of solidification behavior using the Thermocalc simulation (Scheil module). Scheil simulation is helpful for the understanding of binary and multicomponent alloy solidification paths. Since the Scheil module works on the assumption that solid phases are “stationary,” later simulation is directed toward the solidification of the remaining liquid. This kind of simulation involves recently formed solid and liquid phases that must have the mass equilibrium with the residual liquid in the preceding step on an individual level. This mass steadiness requirement drives the solidification track to go through eutectic types of responses.

The solidification path in 304NG is  $L + \alpha \rightarrow L + \alpha + \gamma \rightarrow L + \alpha + \gamma + MnS$  between 1530 and 1750 K temperatures, illustrated in Fig. 6. As discussed above, Ni is an austenite stabilizer in the austenitic steel, decreasing the ferritic molar fraction and solidification path and adding one more austenitic path ( $L + \gamma$ ) in the Scheil module, as shown in Fig. 6a. Ni increases parent matrix stability, which increases the toughness and ductility of alloys. Cr acts as a ferrite stabilizer, so higher Cr content



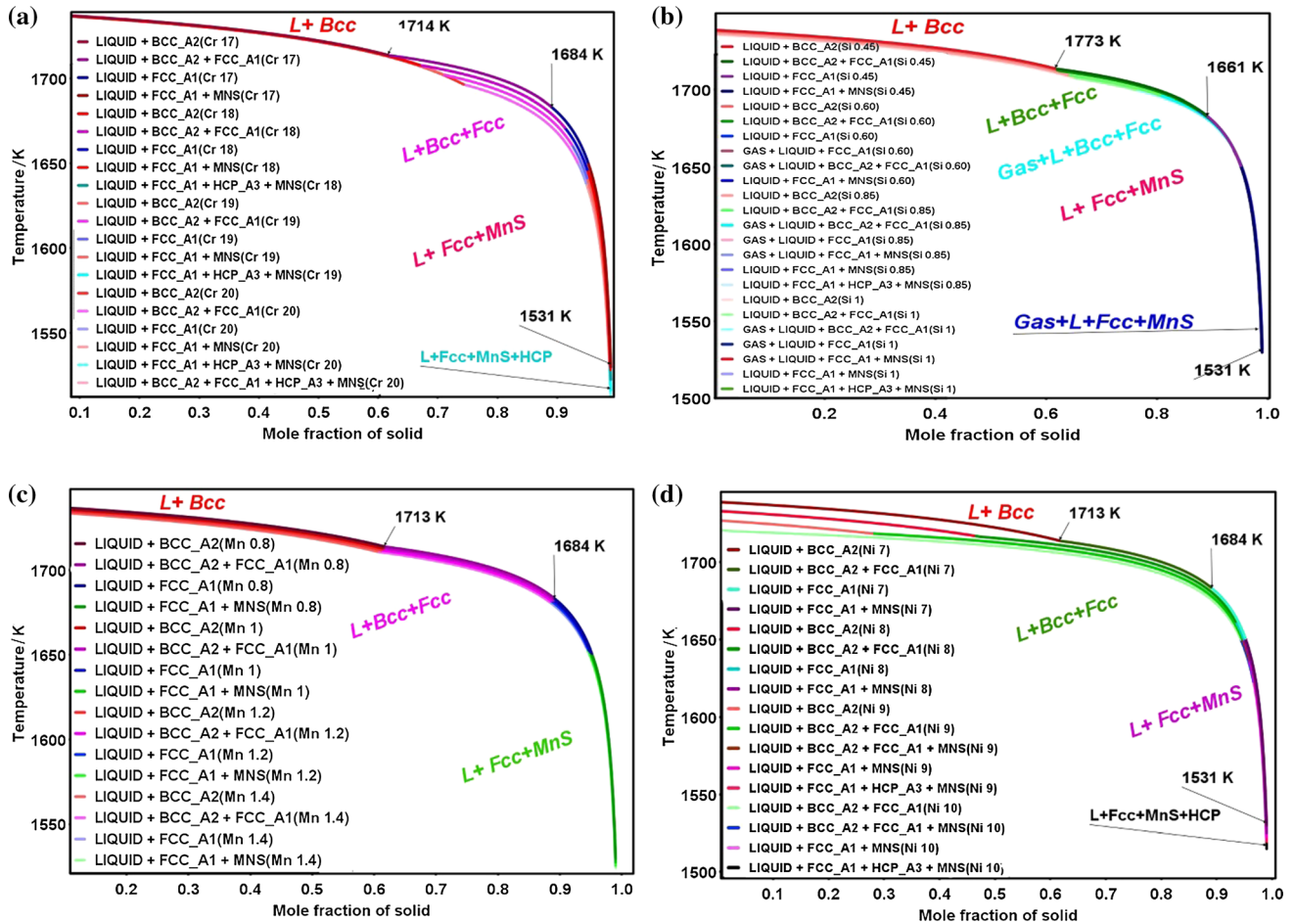


**Figure 6** Scheil solidification diagram for the 304NG alloy composition and its influence on solidifications. **a** effect of Ni, **b** effect of Si, **c** effect of Mn, **d** effect of Cr.

increases the  $L + \alpha$  solidification along with reducing the  $L + \alpha + \gamma$  solidification path. Cr also reduces the length of  $L + \alpha + \gamma$  solidification path because of the austenitic phase and also lowers the solidification temperature of  $L + \alpha + \gamma + MnS$ , as shown in Fig. 6d. In Figure 6b, c, changing Mn and Si content decreases the solidification temperatures for all solidification paths, and it does not affect so much the length of paths or molar fraction of solid w.r.t to changing in both contents in the prescribed range.

### Experimental details during thermomechanical processing (TMP)

Table S1 (supplementary material) shows the actual chemical composition of the nitrogen-controlled 304 stainless steel utilized in this work. First, the

experimental materials were machined into cylindrical specimens size of  $\Phi 10 \text{ mm} \times 15 \text{ mm}$  for the Gleeble 3800 thermal simulator as experimental equipment (Figure S4 in supplementary material). During thermal compression, deformation temperatures range from 900 to 1200 °C along with different strain rates ranging from 0.001 to  $1 \text{ s}^{-1}$ . To maintain a uniform structure, the specimens were heated to 1250 °C at a rate of 5 °C/s for 3 min. After that, specimens cooled down to deformation temperature at a rate of 10 °C/s and then held for 1 min. The Gleeble thermal simulator was also used to feedback and record the temperature fluctuations of the specimens during compression testing by making the temperature uniform and then performing thermal compression at a predetermined strain rate, and the maximum strain value of 0.7. Immediately after compression, the sample is water quenched to preserve the dynamic recrystallization structure

produced during deformation. When the test was completed, then all the specimens were cut in half along the compression direction, and half were taken for grinding and polishing (Figure S4 in supplementary material). The corrosive agent is prepared with 50 ml concentrated hydrochloric acid and 5 ml hydrogen peroxide, and it is corroded at room temperature for 20–25 s. Scanning electron microscope (SEM) was used to examine the microstructure at the cross-sectional plane's center. The grain structure of specimens that have been subjected to hot compression shows different microstructures depending on the processing variables. The entire test procedures are schematically illustrated in Fig. 7.

### Stress–strain curves and toughness calculations.

Figure 8 illustrates true stress–strain curves of 304NG specimens produced at 900–1200 °C with four different strain rates. Flow stress curves typically have comparable characteristics, such as a noticeable work hardening phase at strains less than 0.2, followed by a flow softening stage, and occasionally a stable stage

at high strain zones. These flow patterns are similar to previous low stacking faults energy materials like austenitic steels, demonstrating that DRX can occur during hot deformation [43]. The dislocation density continues to rise, and dislocations rapidly accumulate throughout the work hardening stage, resulting in a rapid increase in stress flow. The effect of work hardening can be somewhat negated during the softening stage by the occurrence of dynamic softening mechanisms such as DRV and DRX [16], which can lead to a drop in flow stress (Figure S5 in supplementary material).

Figure 8a shows the flow stress–strain curve with a constant deformation temperature of 900 °C with various strain rates. It can be perceived that under the condition of different strain rates, from 0.001 to  $1 \text{ s}^{-1}$ , flow stress gradually decreases, and the peak area steadily declines. At lower temperatures, under 900 °C and 1000 °C, and high strain rate, there is no apparent peak stress and steady-state stress, that is, the flow stress has been increasing with the increase of the strain, for the following reasons: At low temperature insufficient atomic activity makes it difficult to nucleate DRX grains, and nucleation is not

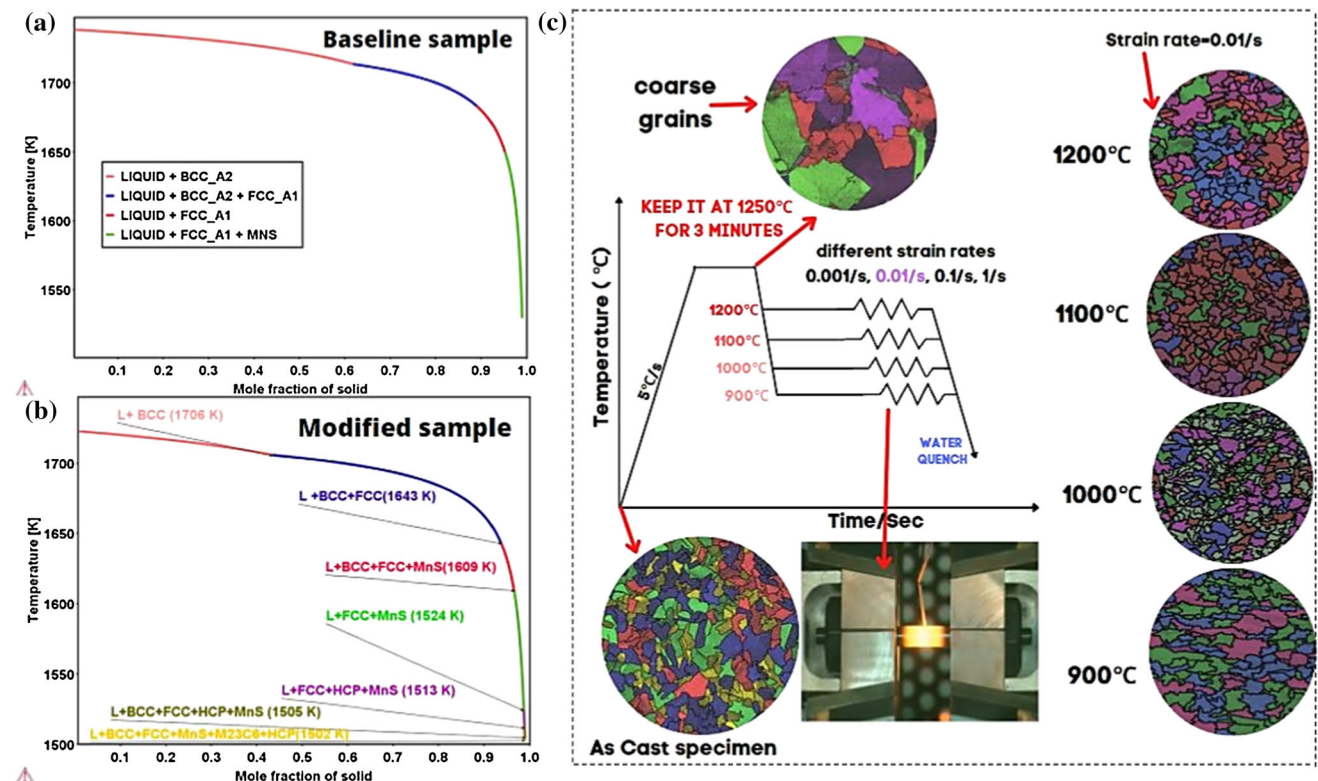


**Figure 7** **a** Predicted solidification path for baseline specimen, **b** predicted solidification path for modified specimen, **c** thermomechanical processing of 304NG steel along with microstructures of 304NG at  $0.01 \text{ s}^{-1}$  strain rate with different temperatures (900 °C to 1200 °C).

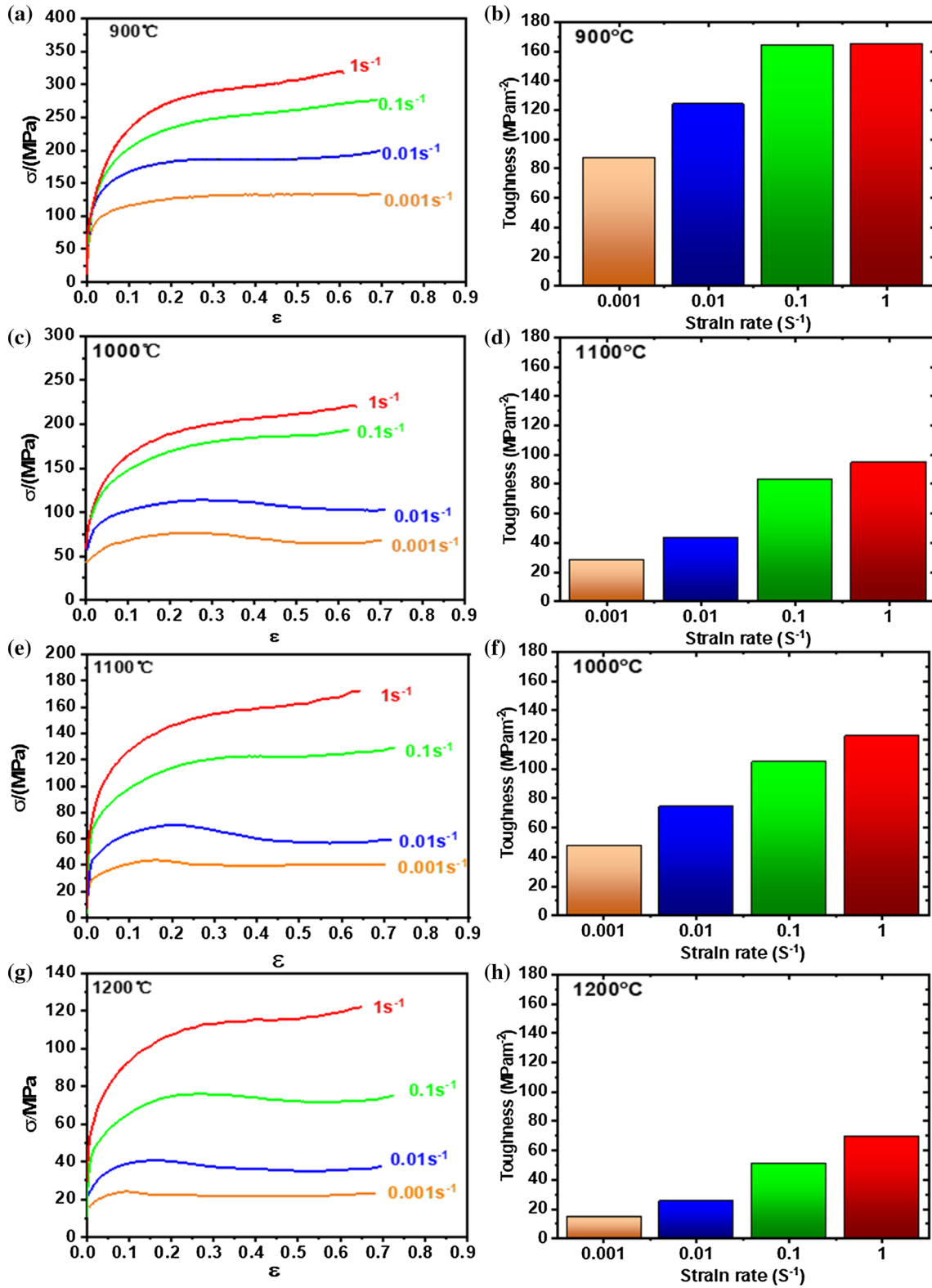


**Figure 8** a Flow stress curves at 900 °C with different strain rates, b toughness calculation at 900 °C with various strain rates, c flow stress curves at 1000 °C with different strain rates, d toughness calculation at 1000 °C with various strain rates,

e flow stress curves at 1100 °C with different strain rates, f toughness calculation at 1100 °C with various strain rates, g flow stress curves at 1200 °C with different strain rates, h toughness calculation at 1200 °C with various strain rates.

conductive to the growth of DRX grains. During TMP compressions, low deformation temperatures and high strain rates make softening effect of dynamic recrystallization low. Higher strain rates and lower temperatures allow for faster energy buildup and reduce mobility at borders, resulting in the nucleation and development of dynamically recrystallized grains and dislocation annihilation. Theoretically, preventing recrystallization or precipitation can improve material strength to some extent, increases the true stress-true strain curve [44]. At the same time, due to high deformation temperatures and low strain rates, more DRX grains nucleate, and grain boundaries are easier to migrate to make DRX grains grow, which enhances softening effect of dynamic recrystallization. The same characteristics are validated in microstructure evolution for other strain rates as the temperature increases (Figure S3 in supplementary material). Because atoms have higher activity at higher temperatures, dislocations are effortlessly merged with vacancies through climbing, and the hardened pinned dislocations are loosened and softened, therefore enhancing the dynamic recovery [45]. Following a significant increase in stress to a peak value, the flow stress declines into a steady-state regime with a variable softening rate, signaling the start of DRX. Furthermore, it is reasonable to deduce that the stress evolution with strain follows three distinct steps based on stress-strain curves. During the first stage, when work hardening (WH) dominates, flow stress rapidly grows critical. In the second stage, the flow curve grows at a slower rate until it hits a peak or inflection in the work hardening rate, suggesting that thermal softening owing to DRX and dynamic recovery (DRV) becomes increasingly dominant eventually surpassing WH. Three sorts of curve variation tendencies can be generalized at the third stage: decreasing after peak stress and gradually stable state with DRX softening ( $900 \sim 1200 \text{ }^\circ\text{C}$  and  $0.01 \text{ s}^{-1}$  and  $0.001 \text{ s}^{-1}$ ), continuing higher stress level without substantial softening and work hardening ( $900 \sim 1100 \text{ }^\circ\text{C}$  at  $0.01 \text{ s}^{-1}$ ), and growing uninterruptedly with substantial work hardening ( $900 \sim 1200 \text{ }^\circ\text{C}$  at  $1 \text{ s}^{-1}$ ) [46]. As a result, the traditional flow curve with DRX softening, consisting of a single peak followed by a steady-state flow as a plateau, is more noticeable at higher temperatures and lower strain rates. Because a higher DRX softening rate slows work hardening at lower strain rates and higher temperatures, the peak stress

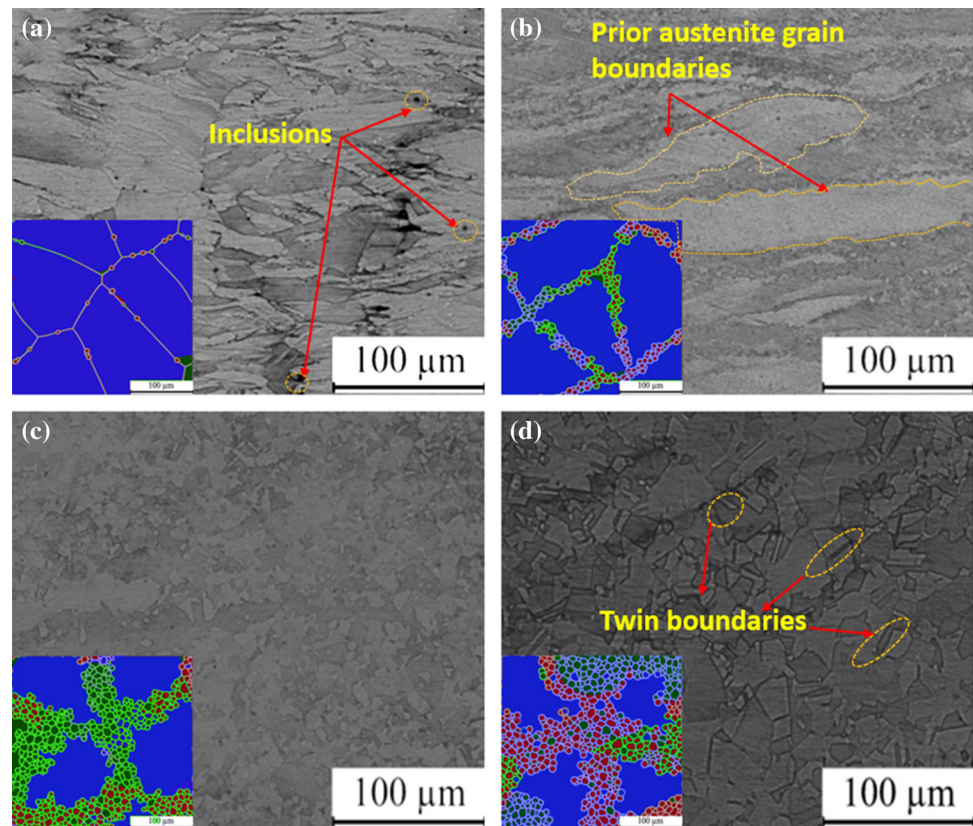
and the start of steady-state flow are shifted to lower strain levels (Figure S5 in supplementary material) [47]. The consumed dislocations by DRX are strongly connected to the lowering of flow stress.

Figure 8b, d, f, and h illustrates the toughness calculation of all specimens by integrated stress-strain values originated by the Gleeble simulator. In the first part of this work, computational optimization of the toughness by eliminating hard particles that fracture easily and introducing ductile barriers to the propagation of cracks were discussed regarding CALPHAD strategies. In the second part, improved strength-toughness combinations are discussed experimentally by grain refinement during hot deformation of austenitic steel specimens. Figure 8 illustrates that low-temperature deformation has high toughness values than high-temperature deformations. The growth of DRX grain reduces the toughness because DRX grain size increases or coarsens, as illustrated in Fig. 9.

### Microstructural evolution during TMP

The microstructures of all specimens subjected to  $\varepsilon = 0.7$  with numerous strain rates and various deformation temperatures are presented in Figure S3 (supplementary material). A wavy nature can be observed in the grain boundaries for all deformation conditions. Fig. S3 (supplementary material) also shows multiple annealing twins in many specimens, especially as-cast and high-temperature deformation specimens. Twins are generated by a specific sort of shearing that occurs inside the grain as a result of plastic deformation. The imposed processing parameters, such as strain, temperature, and strain rate influence the kinetics of DRX. As illustrated in Fig. S3 (supplementary material), DRX grains and their size increase at lower strain rates and high deformation temperature. The favored DRX nucleation sites are the multiple junctions of the initial grains. It happened due to the ease of creating stress concentrations, and nucleation triggered [48]. At a lower strain rate, increasing deformation temperature increases DRX grain size observed in the microstructure. This is because, in the later stage, both the nucleation of DRX and the development of grains produced by grain boundary migration require time (Fig. 9). It takes longer to compress to 0.7 at a low strain rate, permitting the grains formed by

**Figure 9** The microstructure evolution of 304NG at strain rate  $1.0 \text{ s}^{-1}$  with different transformation temperature a  $900 \text{ }^\circ\text{C}$ , b  $1000 \text{ }^\circ\text{C}$ , c  $1100 \text{ }^\circ\text{C}$ , d  $1200 \text{ }^\circ\text{C}$ .



dynamic recrystallization enough time to grow (Figure S7 in supplementary material). As a result, complete recrystallization occurs at high temperatures and low strain rate ( $0.1 \text{ s}^{-1}$ ). After complete dynamic recrystallization, the structure is rather consistent, and the average grain size is  $40\text{--}60 \text{ }\mu\text{m}$  (Fig. 9).

### Effect of various deformation temperatures on DRX

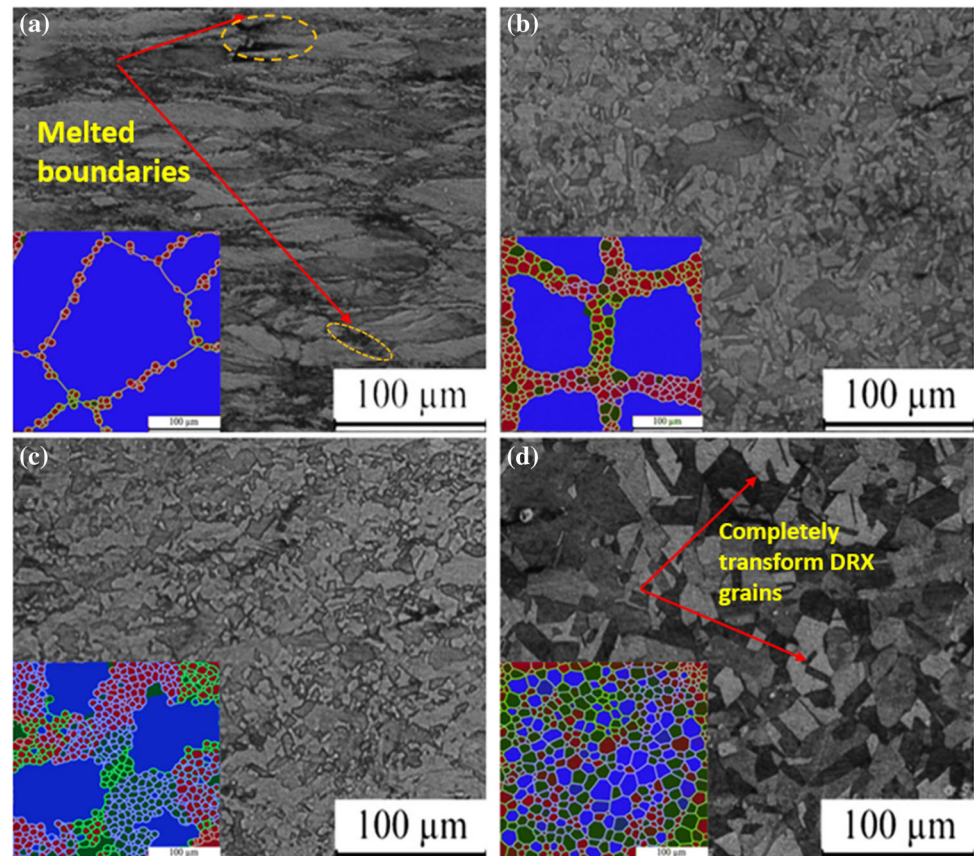
Figures 10 and 11 present a series of micrographs at strain rates of  $1 \text{ s}^{-1}$  and  $0.1 \text{ s}^{-1}$  under different transformation temperatures, respectively. It can be seen from Fig. 10a that when the deformation temperature is  $900 \text{ }^\circ\text{C}$ , only a small part of the DRX grains nucleate along the grain boundaries with the presence of inclusions or pinning particles. Because there is less atomic activity at low temperatures, so the driving force for grain boundary migration is low, and crystal grains are difficult to grow; smaller grains form at the grain boundaries of the retained austenitic grains.

Figure 10a, b illustrates that the original grain structure had not been fully recrystallized, and the grain boundaries are jagged, resulting in

substructures [44]. The grain elongation and saw-tooth of the grain boundaries increase as deformation increases, as grains become more in deformation. As a result of the DRX process, refined grains arise. However, because the driving force of grain boundary migration is less at low temperatures, and crystal grains are difficult to grow, more smaller grains formed at the grain boundaries of the initial crystal grains [7] illustrated in Fig. 12b.

Figure 11 shows the microstructure of 304NG steel specimens at different deformation temperatures at a strain rate of  $1.0 \text{ s}^{-1}$ . Figure 11a illustrates that when the deformation temperature is  $900 \text{ }^\circ\text{C}$ , only a small part of dynamic recrystallization occurs, and new DRX grains nucleate along the grain boundaries. In Figs. 11a, b, c, original grains are still retained at  $900 \text{ }^\circ\text{C}$ ,  $1000 \text{ }^\circ\text{C}$ , and  $1100 \text{ }^\circ\text{C}$  showing incomplete recrystallization along with melted grain boundaries. As the temperature rises, more DRX grains nucleate around the boundaries. At  $1200 \text{ }^\circ\text{C}$  in Fig. 11d, DRX phenomenon has entirely occurred, and the entire structure is evenly distributed with equiaxed DRX grains.

**Figure 10** The microstructure evolution of 304NG at strain rate  $0.1 \text{ s}^{-1}$  with different transformation temperature **a** 900 °C, **b** 1000 °C, **c** 1100 °C, **d** 1200 °C.



It was observed that when the deformation temperature amplified, the volume proportion of DRX grains also increased, implying that DRX behavior happened more efficiently at higher deformation temperatures, as shown in Figs. 11a, b, c, d. At higher deformation temperatures, this effect is linked to a decreased driving force and increased grain boundary mobility. The distribution and density of dislocations, on the other hand, are hypothesized to affect the occurrence of DRX [49], as illustrated in Fig. 12b. Dislocation slip, climb, annihilation, and vacancy diffusion rate increase as the deformation temperature rises, resulting in simpler activation of dynamic recovery and even dynamic recrystallization to overcome hardening [50].

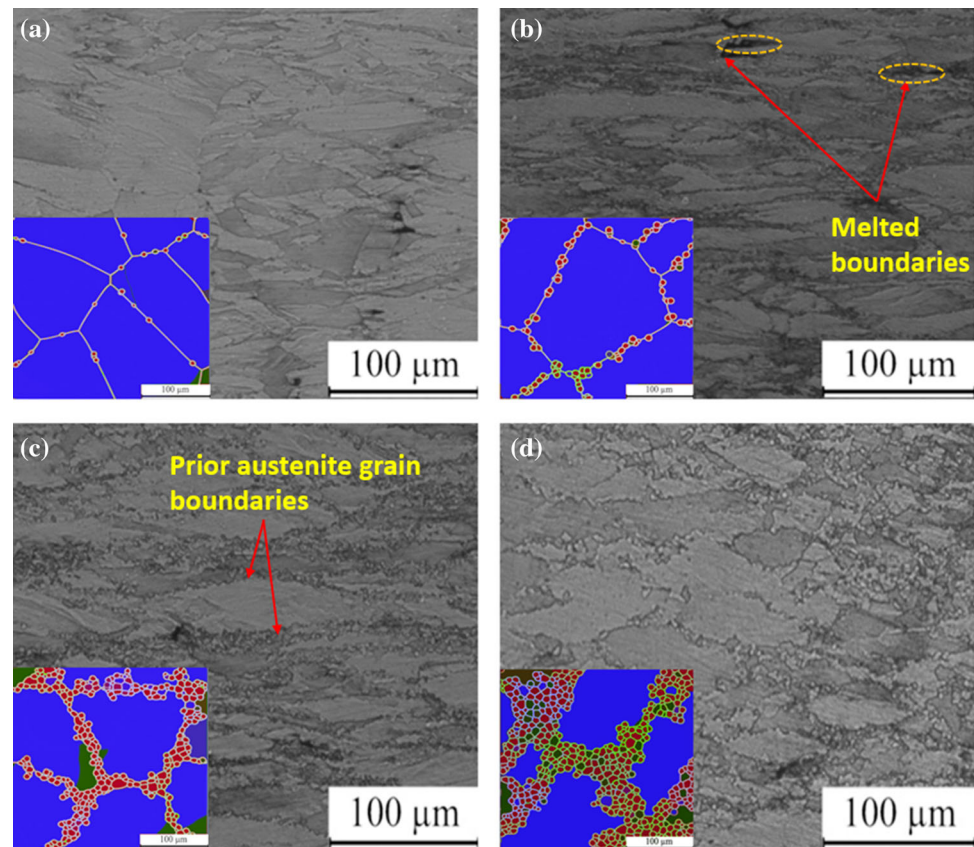
### Effect of various strain rates on DRX

Figures 13 and 14 illustrate a series of microstructures at 900 °C and 1000 °C with different strain rates, respectively. During the compression process at 900 °C, the original structure has not been completely recrystallized, and some initial grains are retained. As the strain rate decreases, more dynamic

recrystallization occurs, and it can be seen that the initial grains gradually decrease and the DRX grains increase. There is enough time for dynamic recrystallization nucleation and grain formation at a lower strain rate. The microstructure illustrated in Figs. 13a, b exhibits sluggish DRX kinetics.

The critical dislocation density reduces as the deformation temperature rises, decreasing the critical strain necessary for DRX to occur [51]. Figure 14 shows the microstructures of specimens with various strain rates at 1000 °C. It has been observed that due to strain rate decreases, the more dynamic recrystallization occurs, initial grains gradually decrease, and DRX grains increase. At 1000 °C, the driving force for migration of grain boundary is higher, and the grains are easier to grow. However, because there is lesser atomic activity at low temperatures, the driving force for migration of grain boundary is reduced, and crystal grains are difficult to grow. It can be seen that the recrystallized grain size at 1000 °C is greater than at 900 °C. At the same time, there are only a small amount of large deformed grains, and fewer original grains are remaining. The recrystallized grains

**Figure 11** The microstructure evolution of 304NG at 900 °C with different strain rates **a** 1 s<sup>-1</sup> **b** 0.1 s<sup>-1</sup> **c** 0.01 s<sup>-1</sup> **d** 0.001 s<sup>-1</sup>.



gradually replace the original grain structure, making the softening effect more obvious. While comparing Figs. 13 and 14, it can be seen that the strain rate drives the DRX process. In another sense, the strain rate significantly impacts the size and volume fraction of DRX grains. When the strain rate is reduced, the volume % and size of DRX grains rise. This occurs because there is enough energy buildup to reduce the driving force at a lower strain rate, increasing the DRX process. DRX, on the other hand, is considered to be triggered by the alloys' propensity for distortion during deformation.

As a result of the reduced strain rate, the alloy atoms have enough time to completely diffuse, consequentially in the release of sufficient distortion potentials to drive the DRX process nucleation. Grain boundary serration and bulging are often aided by a low strain rate, allowing grain boundary movement and DRX formation [52].

Furthermore, the DRX process appears to be speeding up in a high strain rate environment. High strain rates encourage the buildup of dislocations and stored energy, allowing critical dislocation density to be achieved. Softening during hot deformation

resulted from the generation of discontinuous DRX, which is not found at higher strain rates. DRX refines microstructure in a unique way as a consequence. Most critically, twinning during grain expansion necessitates boundary migration. Twinning as a result of growth accidents accelerated growth and leads to nucleation, affecting DRX kinetics [8]. In these low SFE alloys, twin boundaries formed by heat deformation or annealing play a crucial role. The creation of twin boundaries is not only a result of the recrystallization structure, but also plays an integral part in the recrystallization process. The production of twins, which speeds the separation of bulged sections from the original grain boundaries, was expected to improve the DRX of austenite stainless steels [7, 53]. Dislocations tangle and interact inside deformed grains as the strain rate increases, causing slip mechanisms to hamper. As a result, substructures of micro-bands with high-dislocation density are formed, which is advantageous in light of the fast-increasing misorientation of boundaries. The bulging process is unlikely to progress when the pre-existing grain boundaries are entirely covered by new grains [7]. Internal tensions rise when the rate of dislocation

**Figure 12** The microstructure evolution of 304NG at 1000 °C with different strain rates **a**  $1 \text{ s}^{-1}$  **b**  $0.1 \text{ s}^{-1}$  **c**  $0.01 \text{ s}^{-1}$  **d**  $0.001 \text{ s}^{-1}$ .

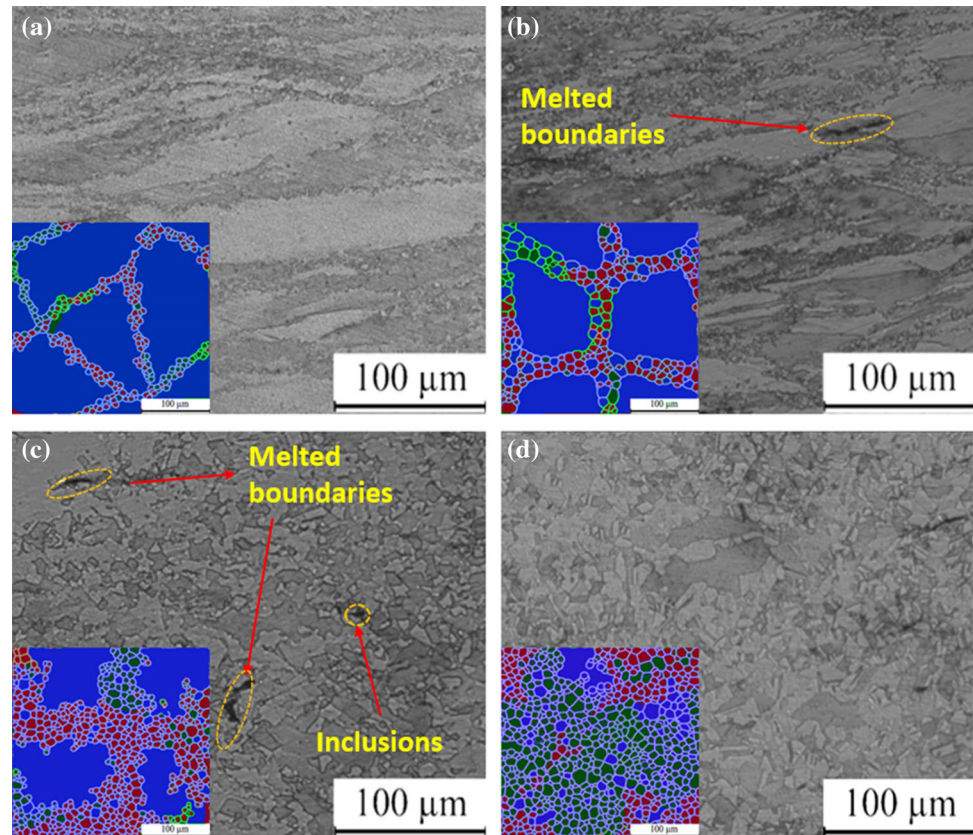
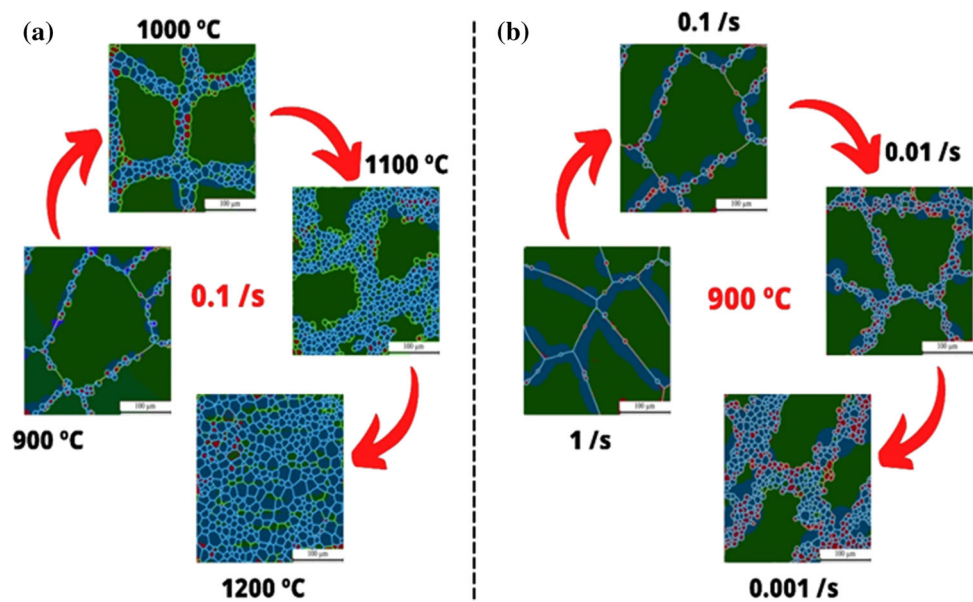


**Figure 13** **a** Proposed DRX grains evolution of 304NG at  $0.1 \text{ s}^{-1}$  with different deformation temperatures and **b** proposed DRX grains evolution pattern of 304NG at 900 °C with different strain rates.



accumulation during deformation exceeds the rate of dislocation relaxation. The dynamic recovery of austenitic materials induced by dislocation cross-slip and ascent is recognized to be insufficient to compensate for the work hardening caused by low SFE [54].

Figure 9 illustrates the grain size distribution of specimens at three stages: as-cast specimen, at 1250 °C (coarse grains), and fully recrystallized form (DRX grains). As a result, DRX is favored during hot deformation, which occurs in the low strain rate zone.



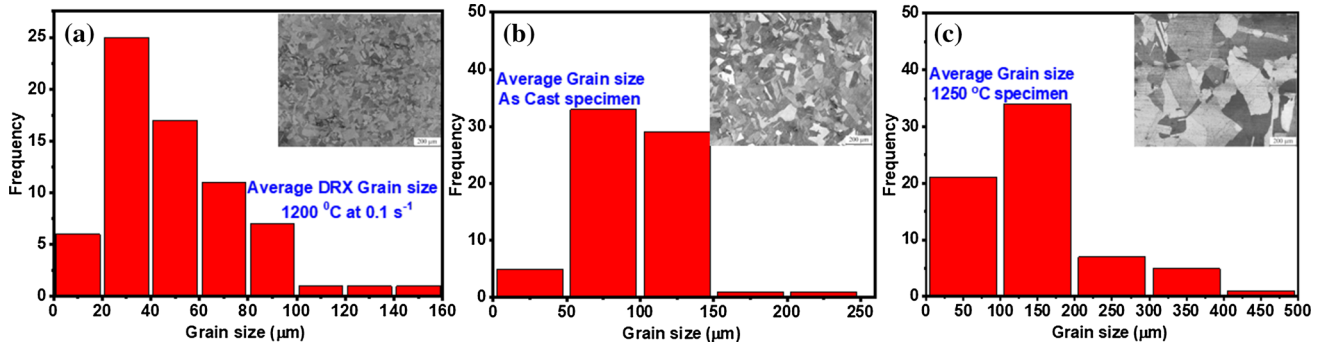


**Figure 14** a Grain size distribution of 304NG at  $0.1 \text{ s}^{-1}$ ,  $1200 \text{ }^{\circ}\text{C}$ , b grain size distribution of 304NG as-cast specimen, c Grain size distribution of 304NG at  $1250 \text{ }^{\circ}\text{C}$ .

The nucleation and development of DRX grains can result in the annihilation of dislocations, which reduces the rate of work hardening; as a result, it causes apparent softening. The size and distribution of prior austenite grain, on the other hand, had an impact on toughness. At  $1200 \text{ }^{\circ}\text{C}$  at various strain rates, Figure S7a (supplementary material) shows a typical “S”-shaped dynamic recrystallization fraction curve. The ultimate recrystallization fraction is 0.98 when the strain rate is  $1.0 \text{ s}^{-1}$ , and it eventually reaches 1 under other strain rates, demonstrating that complete recrystallization has occurred at low strain. The dynamic recrystallization fraction curves at various temperatures with a strain rate of  $0.01 \text{ s}^{-1}$  are shown in Figure S7b in supplementary material. The final recrystallization fraction at  $900 \text{ }^{\circ}\text{C}$  is only about 0.8, indicating that this specimen is not totally recrystallized, which is consistent with the microstructural graph at this temperature. These findings are in line with the findings of microstructural investigations (Figures S3 supplementary material). At  $1000 \text{ }^{\circ}\text{C}$ , the final recrystallization fraction was 0.91, rising to 1 at  $1100 \text{ }^{\circ}\text{C}$  and  $1200 \text{ }^{\circ}\text{C}$ , demonstrating that complete dynamic recrystallization was placed at high deformation temperatures.

## Discussion

Based on the discussions above, two things were proposed, (1) optimum alloying conditions and (2) optimum thermomechanical process for refined grains of 304NG alloy with a high toughness-strength combination. The reason for changing the composition of alloying elements like Cr, Si, Mn, and Ni to control the mechanical properties by phase

transformations of alloy, i.e.,  $\text{M}_{23}\text{C}_6$ , Sigma, and G-phase, is to minimize or optimize according to the requirement of the application. In 1st part, according to Fig. 2, increasing Cr content also increases  $\text{M}_{23}\text{C}_6$ , and  $\sigma$  phase, which is detrimental for toughness, so we use the minimized value of Cr. Ni decreases molar fraction of the Sigma phase, stabilizes the parent phase, and reduces the G-phase, so it could be fruitful to use high content ( $\sim 9 \text{ wt}\%$ ) of Ni for better toughness. As discussed above in Fig. 4, Mn is a suitable replacement for Ni because it also stabilizes the austenite phase, so medium Mn content ( $\sim 1.05 \text{ wt}\%$ ) is more fruitful for RPV application requirements. Silicon contents increase G-phase and Sigma phase detrimental to the toughness of alloy, By eliminating G-phase through decreasing the content of Si ( $0.45 \text{ wt}\%$ ) also affects the toughness of alloy.

In the second part, DRX mechanism in the high or low strain rate regime along various deformation temperatures was developed based on the flow characteristics and microstructure development illustrated in Fig. 12. As discussed above, discontinuous DRX is favored during hot deformation, which occurs at a low strain rate. The annihilation of dislocations can occur as a result of the nucleation and development of DRX grains, lowering the work hardening rate and resulting in apparent softening. Dislocations tangle and interact inside deformed grains as the strain rate rises, obstructing slip mechanisms. The initial as-cast specimen exhibits annealing twins shown in Figure S3 (supplementary material). The dynamic recovery of  $\gamma$ -FCC materials induced by dislocation cross-slip and climb is well known to be insufficient to compensate for the work hardening caused by low stacking fault energy. As a result, high-dislocation density micro-band

substructures are generated, which aid the quick misorientation of grain boundaries. Furthermore, high strain rate regimes with high deformation temperatures are linked to uniform and refined microstructures (Fig. 11d). The thermal energy inside the deformed sample is modest at lower temperatures and strain rates (900 °C and 0.001 s<sup>-1</sup>). The pinning effect is barely overcome by dislocation at the pinning point when performing cross-sliding and climbing actions, resulting in increased dislocation at the pinning point (Fig. 10). Simultaneously, the substructures are produced, but the dynamic recovery does not provide enough thermal energy for them to nucleate. As a result, at lower temperatures, the substructures are smaller and more tightly packed than at higher temperatures, and the recrystallized grains are significantly finer, as seen in Fig. 11d. Furthermore, at lower temperatures, the number of substructures with many dislocations is greater than at higher temperatures (Fig. 11a and d). The strategy employed in this study provides the way for the alloy composition adjustment of 304NG in order to enhance this alloy's toughness–strength ratio and creep resistance in a variety of applications.

## Conclusion

This study suggested the CALPHAD-based computational method for optimizing the 304NG compositions according to phase transformations and mechanical properties such as hardness and strength–toughness combination for high-temperature applications. The following is a summary of the key findings:

1. The CALPHAD strategy was used to produce 304NG industrial steel with low Carbon and Nitrogen composition (Table S1), with alloy design standards that included excellent strength–toughness combination, castability, and formability. The specified steel was cast, then thermo-mechanically processed to generate refined grains to optimize the strength–toughness ratio.
2. Primary recrystallized grains developed at low strain rates. A further rise in strain causes recrystallized grains to distort. Primary recrystallized grains can act as deformed grains, resulting in additional recrystallized grains in their surroundings.
3. Deformation temperature and strain rate influenced DRX kinetics and austenite grain size in 304NG steel; the size of DRX grains after complete recrystallization increased as high deformation temperature and low strain rates.
4. The network of inclusions and pinning particles is entirely broken and effectively diffused into the matrix phase at the same strain rate, with an increase in deformation temperature. Because the diffusion rate rises with increasing temperature, grain boundaries are less likely to be disrupted during hot deformation and accelerated grain boundary migration.
5. Discontinuous DRX occurred during hot deformation in the low strain rate region (0.001–0.1 s<sup>-1</sup>), which resulted in the nucleation of new grains and subsequent grains development. The development of both strain-induced grains and twin boundaries aided the bulging process of nucleation. Twin boundaries are produced mainly during the growth of DRX grains developmental stage. This type of DRX process was accelerated in this regime due to the decrease in strain rate along with high deformation temperature. As a result, more twin boundaries were created during grain development.

## Acknowledgements

The authors would like to express their gratitude to M.E. Li, Professor Sun of Xi'an Jiaotong University for helpful discussions and revision. Also thankful to Karolina Mrozicki for helping to remove English or grammatical mistakes in paper. The authors are thankful to the National Natural Science Foundation of China for financial assistance [grant numbers 51375364].

## Declarations

**Conflict of interest** The authors declare that they have no known competing financial interests or personal relationships that could have appeared to influence the work reported in this paper.

**Supplementary Information:** The online version contains supplementary material available at <http://doi.org/10.1007/s10853-022-07933-y>.

## References

- [1] Deng P, Peng Q, Han EH, Ke W, Sun C, Jiao Z (2017) Effect of irradiation on corrosion of 304 nuclear grade stainless steel in simulated PWR primary water. *Corros Sci* 127:91–100. <https://doi.org/10.1016/j.corsci.2017.08.010>
- [2] Okada O, Nakata K, Kasahara S (1999) Effects of thermal sensitization on radiation-induced segregation in type 304 stainless steel irradiated with He-ions. *J Nucl Mater* 265:232–239. [https://doi.org/10.1016/S0022-3115\(98\)00733-8](https://doi.org/10.1016/S0022-3115(98)00733-8)
- [3] Deng P, Peng Q, Han EH (2021) Grain boundary oxidation of proton-irradiated nuclear grade stainless steel in simulated primary water of pressurized water reactor. *Sci Rep* 11:1–9. <https://doi.org/10.1038/s41598-020-80600-x>
- [4] Deng P, Peng Q, Han EH, Ke W (2017) Effect of the amount of cold work on corrosion of type 304 nuclear grade stainless steel in high-temperature water. *Corrosion* 73:1237–1249. <https://doi.org/10.5006/2436>
- [5] Li C, Shu G, Liu Y, Huang Y, Chen J, Duan Y, Liu W (2018) Effects of neutron irradiation on resistivity of reactor pressure vessel steel. *J Nucl Mater* 499:446–450. <https://doi.org/10.1016/j.jnucmat.2017.12.007>
- [6] Martin M, Weber S, Theisen W, Michler T, Naumann J (2011) Effect of alloying elements on hydrogen environment embrittlement of AISI type 304 austenitic stainless steel. *Int J Hydrog Energy* 36:15888–15898. <https://doi.org/10.1016/j.ijhydene.2011.09.013>
- [7] Wang X, Wang D, Jin J, Li J (2019) Effects of strain rates and twins evolution on dynamic recrystallization mechanisms of austenite stainless steel. *Mater Sci Eng A* 761:138044. <https://doi.org/10.1016/j.msea.2019.138044>
- [8] Zhang H, Zhang K, Jiang S, Lu Z (2015) The dynamic recrystallization evolution and kinetics of Ni-18.3Cr-6.4Co-5.9W-4Mo-2.19Al-1.16Ti superalloy during hot deformation. *J Mater Res* 30:1029–1041. <https://doi.org/10.1557/jmr.2015.78>
- [9] Yasuoka M, Wang P, Zhang K, Qiu Z, Kusaka K, Pyoun YS, Murakami RI (2013) Improvement of the fatigue strength of SUS304 austenite stainless steel using ultrasonic nanocrystal surface modification. *Surf Coat Technol* 218:93–98. <https://doi.org/10.1016/j.surfcoat.2012.12.033>
- [10] Tkachev E, Belyakov A, Kaibyshev R (2020) Creep strength breakdown and microstructure in a 9%Cr steel with high B and low N contents. *Mater Sci Eng A* 772:138821. <https://doi.org/10.1016/j.msea.2019.138821>
- [11] Guan K, Xu X, Xu H, Wang Z (2005) Effect of aging at 700 °C on precipitation and toughness of AISI 321 and AISI 347 austenitic stainless steel welds. *Nucl Eng Des* 235:2485–2494. <https://doi.org/10.1016/j.nucengdes.2005.06.006>
- [12] Li J, Zhang C, Jiang B, Zhou L, Liu Y (2016) Effect of large-size M23C6-type carbides on the low-temperature toughness of martensitic heat-resistant steels. *J Alloys Compd* 685:248–257. <https://doi.org/10.1016/j.jallcom.2016.05.294>
- [13] Marulanda JL, Castañeda SI, Pérez FJ (2015) Improvement in resistance to steam oxidation of aluminide-coated AISI 304 and AISI 316 steel produced by chemical vapor deposition in a fluidized bed reactor. *Oxid Met* 84:429–445. <https://doi.org/10.1007/s11085-015-9563-2>
- [14] Gyu S, Ho D, Su S, Gyeom W, Um K, Kim K, Lee S (2017) Effects of Ni and Mn addition on critical crack tip opening displacement (CTOD) of weld-simulated heat-affected zones of three high-strength low-alloy (HSLA) steels. *Mater Sci Eng A* 697:55–65. <https://doi.org/10.1016/j.msea.2017.04.115>
- [15] El Wahabi M (2005) Effect of initial grain size on dynamic recrystallization in high purity austenitic stainless steels. *Acta Mater* 53:4605–4612. <https://doi.org/10.1016/j.actamat.2005.06.020>
- [16] Marchattiar A, Sarkar A, Chakravarty JK, Kashyap BP (2013) Dynamic recrystallization during hot deformation of 304 austenitic stainless steel. *J Mater Eng Perform* 22:2168–2175. <https://doi.org/10.1007/s11665-013-0496-0>
- [17] Dudás Z (2007) Comparison of measured phase volumes with calculated ones created by TTT-CCT diagram transformation. *Mater Sci Forum* 537–538:497–504. <https://doi.org/10.4028/www.scientific.net/msf.537-538.497>
- [18] Sarizam M, Komizo Y (2014) Effects of holding temperature on bainite transformation in Cr-Mo steel. *J Mech Eng Sci* 7:1103–1114. <https://doi.org/10.15282/jmes.7.2014.9.0107>
- [19] Falkenreck T, Kromm A, Böllinghaus T (2018) Investigation of physically simulated weld HAZ and CCT diagram of HSLA armour steel. *Weld World* 62:47–54. <https://doi.org/10.1007/s40194-017-0511-4>
- [20] Schillé JP, Guo Z, Saunders N, Miodownik AP (2011) Modeling phase transformations and material properties critical to processing simulation of steels. *Mater Manuf Process* 26:137–143. <https://doi.org/10.1080/10426910903153059>
- [21] Wu YX, Sun WW, Gao X, Styles MJ, Arlazarov A, Hutchinson CR (2020) The effect of alloying elements on cementite coarsening during martensite tempering. *Acta Mater*. <https://doi.org/10.1016/j.actamat.2019.11.040>

- [22] H. Ma, P. Fan, Q. Zhang, Y. Zuo, T. Zhu, Y. Zheng, A. Wen, R. Bai, B. Cui, L. Chen, W. Jiang, X. Cao, B. Wang, S. Zhu, D. Yuan, Irradiation Hardening and Indentation Size Effect of the 304NG Stainless Steels After Triple Beam Irradiation, Springer Singapore, 2018. [https://doi.org/10.1007/978-981-13-0158-2\\_21](https://doi.org/10.1007/978-981-13-0158-2_21).
- [23] Kang Y, Zhang G, Xu H, Niu J (2022) Effect of phosphorus on interface characterization of steel–copper bimetals in solid–liquid composite casting. *Mater Today Commun* 30:103037. <https://doi.org/10.1016/j.mtcomm.2021.103037>
- [24] Gupta L, Maji BC, Neogy S, Singh RN, Krishnan M (2022) Precipitation behaviour of 20MnMoNi55 RPV steel in the temperature range of 630–670 °C. *Mater Today Commun* 30:103096. <https://doi.org/10.1016/j.mtcomm.2021.103096>
- [25] Lee KH, Suh JY, Huh JY, Park DB, Hong SM, Shim JH, Jung WS (2013) Effect of Nb and Cu on the high temperature creep properties of a high Mn-N austenitic stainless steel. *Mater Charact* 83:49–57. <https://doi.org/10.1016/j.mtchar.2013.05.015>
- [26] Maalekian M (2007) Christian doppler laboratory for early stages of precipitation the effects of alloying elements on steels (I). *Eff Alloy Elem Steels* 1:36. [https://doi.org/10.1016/S0026-2714\(98\)00110-3](https://doi.org/10.1016/S0026-2714(98)00110-3)
- [27] Wang YQ, Han J, Wu HC, Yang B, Wang XT (2013) Effect of sigma phase precipitation on the mechanical and wear properties of Z3CN20.09M cast duplex stainless steel. *Nucl Eng Des* 259:1–7. <https://doi.org/10.1016/j.nucengdes.2013.02.037>
- [28] Lo KH, Shek CH, Lai JKL (2009) Recent developments in stainless steels. *Mater Sci Eng R Rep* 65:39–104. <https://doi.org/10.1016/j.mser.2009.03.001>
- [29] Schäfer L (1998) Influence of delta ferrite and dendritic carbides on the impact and tensile properties of a martensitic chromium steel. *J Nucl Mater* 258–263:1336–1339. [https://doi.org/10.1016/S0022-3115\(98\)00200-1](https://doi.org/10.1016/S0022-3115(98)00200-1)
- [30] Wang W, Wang R, Dong A, Zhu G, Wang D, Zhou W, Pan W, Shu D, Sun B (2019) Creep behaviors of MC carbide reinforced nickel based composite. *Mater Sci Eng A* 756:11–17. <https://doi.org/10.1016/j.msea.2019.04.010>
- [31] Kolli S, Javaheri V, Ohligschläger T, Kömi J, Porter D (2020) The importance of steel chemistry and thermal history on the sensitization behavior in austenitic stainless steels: experimental and modeling assessment. *Mater Today Commun* 24:101088. <https://doi.org/10.1016/j.mtcomm.2020.101088>
- [32] Niessen F (2018) Austenite reversion in low-carbon martensitic stainless steels—a CALPHAD-assisted review. *Mater Sci Technol (United Kingdom)* 34:1401–1414. <https://doi.org/10.1080/02670836.2018.1449179>
- [33] Abdullah MR, Hongneng C, Liang F (2021) Strategies regarding high-temperature applications w.r.t strength, toughness, and fatigue life for SA508 Alloy. *Materials* 14(8):1953. <https://doi.org/10.3390/ma14081953>
- [34] Nam WJ, Choi HC (1997) Effects of silicon, nickel, and vanadium on impact toughness in spring steels. *Mater Sci Technol* 13:568–574. <https://doi.org/10.1179/mst.1997.13.7.568>
- [35] Chen QY, Chen J, Ren JK, Wang ZH, Liu ZY (2020) Effect of Si content on microstructure and cryogenic toughness of heat affected zone of low nickel steel. *Mater Sci Eng A* 771:138621. <https://doi.org/10.1016/j.msea.2019.138621>
- [36] S. Lin, CALPHAD-assisted morphology control of manganese sulfide inclusions in free-cutting steels, (2016) 94. <https://doi.org/10.1016/j.jallcom.2018.11.290>.
- [37] Shi W, Yang S, Li J (2018) Correlation between evolution of inclusions and pitting corrosion in 304 stainless steel with yttrium addition. *Sci Rep* 8:1–9. <https://doi.org/10.1038/s41598-018-23273-x>
- [38] Xue J, Tao G, Tang C, Xu N, Li F, Yin C (2020) Effect of siliconizing with molten salt on the wear resistance and corrosion resistance of AISI 302 stainless steel. *Surf Coat Technol* 382:125217. <https://doi.org/10.1016/j.surfcoat.2019.125217>
- [39] Cha SC, Hong SH, Kim I, Kim MY, Park J, Suh JY, Shim JH, Jung WS (2016) CALPHAD-based alloy design for advanced automotive steels - Part I: Development of bearing steels with enhanced strength and optimized microstructure, *Calphad Comput. Coupling Phase Diagr Thermochem* 54:165–171. <https://doi.org/10.1016/j.calphad.2016.04.007>
- [40] Sourmail T (2001) Precipitation in creep resistant austenitic stainless steels. *Mater Sci Technol* 17:1–14. <https://doi.org/10.1179/026708301101508972>
- [41] Shuro I, Kuo HH, Sasaki T, Hono K, Todaka Y, Umemoto M (2012) G-phase precipitation in austenitic stainless steel deformed by high pressure torsion. *Mater Sci Eng A* 552:194–198. <https://doi.org/10.1016/j.msea.2012.05.030>
- [42] Guo XF, Ni YY, Gong JM, Geng LY, Tang JQ, Jiang Y, Jia XK, Yang XY (2017) Formation of G-phase in 20Cr32Ni1Nb stainless steel and its effect on mechanical properties. *Acta Metall Sinica (English Lett)* 30(9):829–839. <https://doi.org/10.1007/s40195-017-0589-0>
- [43] de Abreu HFG, de Carvalho SS, de Lima Neto P, dos Santos RP, Freire VN, de Silva PMO (2007) SSM tavares, deformation induced martensite in an AISI 301LN stainless steel: characterization and influence on pitting corrosion resistance. *Mater Res* 10:359–366. <https://doi.org/10.1590/s1516-14392007000400007>
- [44] Ivanova N, Gugleva V, Dobрева M, Pehlivanov I, Stefanov S, Andonova V (2016) Characterization for dynamic

- recrystallization kinetics based on stress-strain curves, *Intech*. i 13
- [45] Que Z, Heczko M, Kuběna I, Seifert HP, Spätig P (2020) Microstructural characterization of the synergic effects of dynamic strain ageing and hydrogen on fracture behaviour of low-alloy RPV steels in high-temperature water environments. *Mater Charact* 165:110405. <https://doi.org/10.1016/j.matchar.2020.110405>
- [46] Xiao ZB, Huang YC, Liu Y (2016) Modeling of flow stress of 2026 Al Alloy UNDER hot compression. *Adv Mater Sci Eng* 2016:28–32. <https://doi.org/10.1155/2016/3803472>
- [47] Huang K, Logé RE (2016) A review of dynamic recrystallization phenomena in metallic materials. *Mater Des* 111:548–574. <https://doi.org/10.1016/j.matdes.2016.09.012>
- [48] Cho SH, Kang KB, Jonas JJ (2001) Dynamic, static and metadynamic recrystallization of a Nb-microalloyed steel. *ISIJ Int* 41:63–69. <https://doi.org/10.2355/isijinternational.41.63>
- [49] Li X, Ma X, Subramanian SV, Shang C, Misra RDK (2014) Influence of prior austenite grain size on martensite-austenite constituent and toughness in the heat affected zone of 700MPa high strength linepipe steel. *Mater Sci Eng A* 616:141–147. <https://doi.org/10.1016/j.msea.2014.07.100>
- [50] Stewart GR, Elwazri AM, Vue S, Jonas JJ (2006) Modelling of dynamic recrystallisation kinetics in austenitic stainless and hypereutectoid steels. *Mater Sci Technol* 22:519–524. <https://doi.org/10.1179/026708306X81478>
- [51] Zeng Z, Chen L, Zhu F, Liu X (2011) Dynamic recrystallization behavior of a heat-resistant martensitic stainless steel 403Nb during hot deformation. *J Mater Sci Technol* 27:913–919. [https://doi.org/10.1016/S1005-0302\(11\)60164-3](https://doi.org/10.1016/S1005-0302(11)60164-3)
- [52] Liu J, Chen H (2019) Nucleation and grain boundary evolution in dynamic recrystallization of 316LN steel during hot deformation. *Front Mater* 6:1–8. <https://doi.org/10.3389/fmats.2019.00209>
- [53] Mirzadeh H, Cabrera JM, Najafizadeh A, Calvillo PR (2012) EBSD study of a hot deformed austenitic stainless steel. *Mater Sci Eng A* 538:236–245. <https://doi.org/10.1016/j.msea.2012.01.037>
- [54] Taylor AS, Hodgson PD (2011) Dynamic behaviour of 304 stainless steel during high Z deformation. *Mater Sci Eng A* 528:3310–3320. <https://doi.org/10.1016/j.msea.2010.12.093>

**Publisher's Note** Springer Nature remains neutral with regard to jurisdictional claims in published maps and institutional affiliations.

Springer Nature or its licensor (e.g. a society or other partner) holds exclusive rights to this article under a publishing agreement with the author(s) or other rightsholder(s); author self-archiving of the accepted manuscript version of this article is solely governed by the terms of such publishing agreement and applicable law.